

Research Article

Adaptive Saturated Neural Network Tracking Control of Spacecraft: Theory and Experimentation

Kewei Xia^{1,2}, Taeyang Lee,¹ and Sang-Young Park^{1,2}

¹*Astrodynamics and Control Laboratory, Department of Astronomy, Yonsei University, Seoul 03722, Republic of Korea*

²*Yonsei University Observatory, Yonsei University, Seoul 03722, Republic of Korea*

Correspondence should be addressed to Sang-Young Park; spark624@yonsei.ac.kr

Received 7 August 2019; Accepted 23 September 2019; Published 20 November 2019

Academic Editor: Maj D. Mirmirani

Copyright © 2019 Kewei Xia et al. This is an open access article distributed under the Creative Commons Attribution License, which permits unrestricted use, distribution, and reproduction in any medium, provided the original work is properly cited.

An adaptive saturated neural network (NN) controller is developed for 6 degree-of-freedom (6DOF) spacecraft tracking, and its hardware-in-the-loop experimental validation is tested on the ground-based test facility. To overcome the dynamics uncertainties and prevent the large control saturation caused by the large tracking error at the beginning operation, a saturated radial basis function neural network (RBFNN) is introduced in the controller design, where the approximate error is counteracted by an adaptive continuous robust term. In addition, an auxiliary dynamical system is employed to compensate for the control saturation. It is proved that the ultimate boundedness of the closed-loop system is achieved. Besides, the proposed controller is implemented into a testbed facility to show the final operational reliability via hardware-in-the-loop experiments, where the experimental scenario describes that the simulator is tracking a planar trajectory while synchronizing its attitude with the desired angle. Experimental results illustrate that the proposed controller ensures that the simulator can track a preassigned trajectory with robustness to unknown inertial parameters and disturbances.

1. Introduction

In recent few decades, spacecraft control has been attracting widespread interest because of its typical orbit applications, such as formation flying, construction of space station, and space surveillance and capturing, rendezvous, and docking. Since the highly nonlinear character arising from 6DOF dynamics in the presence of disturbance and parametric uncertainty would bring more difficulties, it is still challenging to design high-performance controllers for spacecraft. However, most previous work has only focused on the controller design without perhaps the most critical experimental validations [1].

In previous studies, different controllers have been found to be related to 6DOF spacecraft control problems, such as PD+ controller [2], sliding surface controller [3], and disturbance observer-based controller [4, 5]. However, controllers in [2–5] have only been carried out in the presence of exact inertial parameters or disturbances (or their bounds). A

number of techniques have been developed to solve the control problems of 6DOF spacecraft with unavailable uncertainties [6–13]. For 6DOF spacecraft operations subject to unknown parameters and disturbances, adaptive controllers [6, 14, 15] are synthesized. In addition, adaptive saturated controllers [7, 8] are designed by using different saturation compensating methods. To achieve 6DOF spacecraft maneuvers in the presence of control saturations and dynamics uncertainties, disturbance observer-based saturated controllers are studied in [9, 10].

The neural network, which is an alternative solution with highly approximate capacity [11], also draws attention to 6DOF spacecraft controls. For formation flying control problems with parametric uncertainties and disturbances, a NN-based adaptive sliding mode controller is proposed in [12]. For cooperative rendezvous and docking maneuvers, a NN-based switching saturated control is investigated in [13]. Besides, adaptive NN controllers are also studied in helicopter [16] and marine surface vessel [17].

Nevertheless, the abovementioned studies have failed to demonstrate the designed controllers by hardware-in-the-loop experimental validations.

To realize the theoretical results in practical applications, the air-bearing ground test facilities have been developed [18, 19] and some controllers have been validated by hardware-in-the-loop experiments [20–26]. For spacecraft operations subject to parametric uncertainties, adaptive controllers are designed and the related experimental validations are conducted on the ground test facilities [20, 21]. For spacecraft operations, PID [22] and LQR [23] controllers are designed and experimentally tested, respectively. In addition, several controllers [24–26] are developed and validated on the testbed facility. Despite the fact that experimental results can be found in [20–26], the NN-based controllers are rarely validated by hardware-in-the-loop experiments in previous results.

This paper seeks to address the controller design for 6DOF spacecraft tracking operations subject to unknown inertial parameters and disturbances. A saturated NN is designed to approximate the unknown dynamics, and the approximate error is counteracted by an adaptive robust compensating term. An auxiliary dynamical system is introduced to ensure the designed controller satisfying the magnitude constraints. The most remarkable result in this work is that the proposed NN saturated controller is validated by hardware-in-the-loop experiments which are conducted on the ASTERIX facility. Compared with the aforementioned works, the main contributions of this paper are threefold. First, in contrast to the NN employed in [12, 13, 16, 17], a saturated NN is developed to approximate the dynamics uncertainties while avoiding the long time saturation arising from the large tracking errors at the beginning of the operation. Second, to satisfy the magnitude constraints of the actuators installed in spacecraft, an auxiliary variable generated by a dynamical system is introduced in the control design. Compared with the dynamical system designed in [17], the proposed one gives a simpler structure which makes it easier to be realized in practical engineering applications. Finally, different from the numerical simulation validation of NN controllers in [12, 13], the proposed controller is experimentally validated on the ASTERIX facility, where the practical impacts including parametric uncertainties, disturbances, and measurement errors are affecting. The experimental results demonstrate that the proposed controller works and that the results meet theoretical predictions, within a margin of error.

The remaining sections are arranged as follows. Mathematical preliminaries are formulated in Section 2. The control problem to be solved is stated in Section 3. The main results including the controller design and stability proof are given in Section 4. Basic hardware characteristics of the ASTERIX facility and experimental results are presented in Section 5. Finally, the conclusions are summarized in Section 6.

2. Preliminaries

2.1. Notations. In what follows, $\|x\|$ denotes the Euclidean norm of a vector $\mathbf{x} \in \mathbb{R}^n$, $\lambda_{\min}(\mathbf{X})$ and $\lambda_{\max}(\mathbf{X})$ denote the

minimum and maximum eigenvalues of a square matrix $\mathbf{X} \in \mathbb{R}^{n \times n}$, respectively. For $\mathbf{x} = [x_1, x_2, x_3]^T \in \mathbb{R}^3$, superscript \times represents the matrix form of the cross product satisfying $\mathbf{x}^\times = [0, -x_3, x_2; x_3, 0, -x_1; -x_2, x_1, 0]$. For $x \in \mathbb{R}$ and positive constants a and b , the saturation function is defined as follows:

$$\text{sat}_{a,b}(x) = \begin{cases} a, & \text{if } x > a, \\ x, & \text{if } -b \leq x \leq a, \\ -b, & \text{if } x < -b. \end{cases} \quad (1)$$

If no confusion arises, $\text{sat}(x)$ always presents $\text{sat}_{a,b}(x)$ throughout this paper. For $\mathbf{x} = [x_1, x_2, \dots, x_n]^T \in \mathbb{R}^n$, define the saturation function vector $\text{sat}(\mathbf{x}) = [\text{sat}(x_1), \text{sat}(x_2), \dots, \text{sat}(x_n)]^T$.

2.2. RBFNN Approximation. Let $f(\mathbf{x}): \mathbb{R}^n \rightarrow \mathbb{R}$ be an unknown smooth function. According to [11], we can approximate $f(\mathbf{x})$ on a compact set $\Omega \subseteq \mathbb{R}^n$ by employing the following RBFNN:

$$f(\mathbf{x}) = \mathbf{w}^T \Phi(\mathbf{x}) + \epsilon, \quad (2)$$

where ϵ is the bounded approximation error, $\mathbf{w} \in \mathbb{R}^l$ is the weight vector, and l is the node number. \mathbf{w} is defined by

$$\mathbf{w} = \arg \min_{\hat{\mathbf{w}}} \left\{ \sup_{\mathbf{x} \in \Omega} |f(\mathbf{x}) - \hat{\mathbf{w}}^T \Phi(\mathbf{x})| \right\}, \quad (3)$$

where $\hat{\mathbf{w}}$ is the estimate of \mathbf{w} , $\Phi(\mathbf{x}) = [\phi_1(\mathbf{x}), \phi_2(\mathbf{x}), \dots, \phi_l(\mathbf{x})]^T: \Omega \rightarrow \mathbb{R}^l$ is the RBF vector, and $\phi_i(\mathbf{x})$ is the Gaussian function satisfying

$$\phi_i(\mathbf{x}) = \exp \left(-\frac{\|\mathbf{x} - \mu_i\|^2}{\eta_i^2} \right), \quad i = 1, 2, \dots, l, \quad (4)$$

with its center $\mu_i \in \mathbb{R}^n$ and its spread $\eta_i > 0$.

3. Problem Formulation

3.1. Reference Coordinate Frames. Assume that the spacecraft and simulator are rigid bodies, respectively. To formulate their dynamics, the following coordinate frames are defined. The Earth inertial frame ($\mathcal{F}_{\mathcal{I}} = \{O, \mathbf{x}_i, \mathbf{y}_i, \mathbf{z}_i\}$): its origin O is located at the Earth center, axes \mathbf{x}_i and \mathbf{z}_i point to the direction of the vernal equinox and toward the north pole, respectively, and three axes satisfy the Right-Hand-Rule (RHR) frame. The spacecraft (desired) body fixed frame $\mathcal{F}_{\mathcal{B}} = \{B, \mathbf{x}_B, \mathbf{y}_B, \mathbf{z}_B\}$ ($\mathcal{F}_{\mathcal{B}0} = \{B_0, \mathbf{x}_{B0}, \mathbf{y}_{B0}, \mathbf{z}_{B0}\}$): its origin B (B_0) coincides with its center of mass (c.m.), and three axes coincide with its three inertial principal axes, respectively. The desired orbit frame (local vertical local horizontal (LVLH) frame) $\mathcal{F}_{\mathcal{L}} = \{L, \mathbf{x}_L, \mathbf{y}_L, \mathbf{z}_L\}$: its origin L is the center of the desired target, \mathbf{x}_L axis points from the earth center to L , \mathbf{z}_L axis is perpendicular to the orbit plane, and \mathbf{y}_L axis is in the orbit plane complying with the RHR. The testbed centred frame $\mathcal{F}_{\mathcal{T}} =$

$\{T, \mathbf{x}_T, \mathbf{y}_T\}$: its origin is the geometric center of the testbed surface, two axes are along the edges of the bed forming an orthogonal plane coordinate frame.

3.2. 6DOF Dynamics Model

3.2.1. Attitude Error Dynamics. The attitude of spacecraft is represented by using Modified Rodrigues Parameters (MRPs) $\sigma \in \{\sigma \in \mathbb{R}^3 \mid \sigma = \hat{\mathbf{n}} \tan(\eta/4)\}$, where $\hat{\mathbf{n}} \in \mathbb{R}^3$ is the principal rotation axis and $\eta \in (-2\pi, 2\pi)$ is the principal rotating angle. According to [27], by introducing a switching condition at the surface $\|\sigma\| = 1$, the unique and nonsingular description can be guaranteed. This further ensures that $0 \leq \sigma^T \sigma \leq 1$. Let σ and σ_d be the MRPs of the spacecraft and the desired, respectively. The error MRPs are given by

$$\tilde{\sigma} = \frac{\sigma_d(\sigma^T \sigma - 1) + \sigma(1 - \sigma_d^T \sigma_d) - 2\sigma_d^* \sigma}{1 + \sigma_d^T \sigma_d \sigma^T \sigma + 2\sigma_d^T \sigma} \quad (5)$$

According to [27], the attitude error kinematics satisfies

$$\dot{\tilde{\sigma}} = \mathbf{G}(\tilde{\sigma})\tilde{\omega}, \quad (6)$$

where $\mathbf{G}(\tilde{\sigma}) = 1/4[(1 - \tilde{\sigma}^T \tilde{\sigma})\mathbf{I}_3 + 2\tilde{\sigma}^\times + 2\tilde{\sigma}\tilde{\sigma}^T]$, $\tilde{\omega} = \omega - \tilde{\mathbf{R}}\omega_d$ is the error angular velocity expressed in frame $\mathcal{F}_{\mathcal{B}}$, ω and ω_d , respectively, represent the angular velocities of the spacecraft and the desired, and $\tilde{\mathbf{R}}$ is the rotation matrix defined as

$$\tilde{\mathbf{R}} \triangleq \mathbf{R}(\tilde{\sigma}) = \mathbf{I}_3 - \frac{4(1 - \tilde{\sigma}^T \tilde{\sigma})}{(1 + \tilde{\sigma}^T \tilde{\sigma})^2} \tilde{\sigma}^\times + \frac{8(\tilde{\sigma}^\times)^2}{(1 + \tilde{\sigma}^T \tilde{\sigma})^2}. \quad (7)$$

In addition, according to [27] and $\dot{\tilde{\mathbf{R}}} = \tilde{\mathbf{R}}\tilde{\omega}^\times$, we have the following attitude error dynamics:

$$\mathbf{J}\dot{\tilde{\omega}} = -\omega^\times \mathbf{J}\omega + \tau + \tau_d + \mathbf{J}(\tilde{\omega}^\times \tilde{\mathbf{R}}\omega_d - \tilde{\mathbf{R}}\dot{\omega}_d), \quad (8)$$

where $\mathbf{J} \in \mathbb{R}^{3 \times 3}$ is the inertia matrix, $\tau \in \mathbb{R}^3$ and $\tau_d \in \mathbb{R}^3$ are the control torque and disturbance torque, respectively.

3.2.2. Orbit Error Dynamics. Let $\tilde{\mathbf{r}} = \mathbf{r} - \delta$ and $\tilde{\mathbf{v}} = \mathbf{v} - \dot{\delta}$ be the position and velocity tracking errors, where $\mathbf{r} = [r_x, r_y, r_z]^T$ is the position vector error between the spacecraft and desired target, \mathbf{v} is the velocity error, and δ is the desired trajectory referenced in frame $\mathcal{F}_{\mathcal{S}}$. In terms of [28], the orbit error kinematics and dynamics satisfy

$$\dot{\tilde{\mathbf{r}}} = \tilde{\mathbf{v}}, \quad (9)$$

$$m\dot{\tilde{\mathbf{v}}} = -m\mathbf{C}_t \mathbf{v} - m\mathbf{n}_t + \mathbf{R}_L^B \mathbf{f} + \mathbf{f}_d - m\dot{\delta}, \quad (10)$$

where m is the mass of the spacecraft,

$$\mathbf{C}_t = 2\dot{\mathbf{v}} \begin{bmatrix} 0 & -1 & 0 \\ 1 & 0 & 0 \\ 0 & 0 & 0 \end{bmatrix}, \quad \mathbf{n}_t = \begin{bmatrix} -\ddot{v}_y - \dot{v}_x^2 + \frac{\mu(r_0 + r_x)}{(r_0 + r_x)^2 + r_y^2 + r_z^2}^{3/2} - \frac{\mu}{r_0^2} \\ \ddot{v}_x - \dot{v}_y^2 + \frac{\mu r_y}{((r_0 + r_x)^2 + r_y^2 + r_z^2)^{3/2}} \\ \frac{\mu r_z}{((r_0 + r_x)^2 + r_y^2 + r_z^2)^{3/2}} \end{bmatrix}. \quad (11)$$

$\mathbf{R}_L^B = \mathbf{R}_L \mathbf{R}^T(\sigma)$ is the rotation matrix from frame $\mathcal{F}_{\mathcal{B}}$ to frame $\mathcal{F}_{\mathcal{S}}$, \mathbf{R}_L is the rotation matrix between frames $\mathcal{F}_{\mathcal{S}}$ and $\mathcal{F}_{\mathcal{S}}$ satisfying

$$\mathbf{R}_L = \begin{bmatrix} c(\Omega_0)c(\theta_0) - s(\Omega_0)s(\theta_0)c(i_0) & s(\Omega_0)c(\theta_0) + c(\Omega_0)s(\theta_0)c(i_0) & s(\theta_0)s(i_0) \\ -c(\Omega_0)s(\theta_0) - s(\Omega_0)c(\theta_0)c(i_0) & -s(\Omega_0)s(\theta_0) + c(\Omega_0)c(\theta_0)c(i_0) & c(\theta_0)s(i_0) \\ s(\Omega_0)s(i_0) & -c(\Omega_0)s(i_0) & c(i_0) \end{bmatrix}, \quad (12)$$

with the true anomaly ν , the radial distance between the desired target and the Earth r_0 , the right ascension of ascending node Ω_0 , the argument of latitude $\theta_0 = \omega_p + \nu$, the argument of perigee ω_p , and the orbit inclination i_0 , $\mathbf{f} \in \mathbb{R}^3$ is the control force in frame $\mathcal{F}_{\mathcal{B}}$, and $\mathbf{f}_d \in \mathbb{R}^3$ is the disturbance force. c and s stand for *cosine* and *sine*, respectively.

3.2.3. Actuator Distribution. Consider that there are N pairs of thrusters installed in the spacecraft controlling of attitude

and orbit simultaneously. Each thruster in one pair is assembled symmetrically with respect to the rotation center for the dynamics. The control torque direction and the spin axis satisfy the right-hand principle. In particular, each pair of thrusters consists of thrusters T_j and P_j , where T_j provides control force along one axis and control torque around another spin axis of frame $\mathcal{F}_{\mathcal{B}i}$ simultaneously and P_j provides the opposite control force and torque generated by T_j . Let $\mathbf{p} \in \mathbb{R}^N$ be the outputs of all the pairs of thrusters

and $\mathbf{A} \in \mathbb{R}^{6 \times N}$ be the distribution matrix. To ensure the control system non-under-actuated case, the distribution matrix should satisfy $\text{rank}(\mathbf{A}) = 6$.

Due to the fact that the thrusters are generally constrained by power supply in practice, we further consider saturations in the command controls. Generally, the saturated control is expressed by using the saturation function $\text{sat}(\cdot)$. In the studied case, we have that $\mathbf{p} = \text{sat}(\xi) = [\text{sat}(\xi_1), \text{sat}(\xi_2), \dots, \text{sat}(\xi_N)]^T$ with

$$\text{sat}(\xi_j) = \begin{cases} \bar{\xi}_j^+, & \text{if } \xi_j > \bar{\xi}_j^+, \\ \xi_j, & \text{if } -\bar{\xi}_j^- \leq \xi_j \leq \bar{\xi}_j^+, \\ -\bar{\xi}_j^-, & \text{if } \xi_j < -\bar{\xi}_j^-, \end{cases} \quad (13)$$

where $\xi \in \mathbb{R}^N$ is the command control, $\bar{\xi}_j^+ > 0$ and $\bar{\xi}_j^- > 0$, $j = 1, 2, \dots, N$, are the magnitude constraints. Let $\mathbf{u} = [\tau^T, (\mathbf{R}_L^B \mathbf{f})^T]^T$ and define $\Delta \xi = \text{sat}(\xi) - \xi$. Then, we have

$$\mathbf{u} = \mathbf{D} \mathbf{A} \text{sat}(\xi) = \mathbf{D} \mathbf{A} (\xi + \Delta \xi), \quad (14)$$

where $\mathbf{D} = \text{diag}(\mathbf{I}_3, \mathbf{R}_L^B)$. In addition, to ensure that the command control of each thrust should be nonnegative, i.e., $T_j, P_j \geq 0, j = 1, 2, \dots, N$, the command control signals are arranged as follows:

$$\begin{cases} T_j = \text{sat}(\xi_j), P_j = 0, & \text{if } \xi_j \geq 0, \\ P_j = -\text{sat}(\xi_j), T_j = 0, & \text{if } \xi_j < 0. \end{cases} \quad (15)$$

3.2.4. 6DOF Error Dynamics. Let $\mathbf{x}_1 = [\tilde{\sigma}^T, \tilde{\mathbf{r}}^T]^T$ and $\mathbf{x}_2 = [\tilde{\omega}^T, \tilde{\mathbf{v}}^T]^T$. In view of equation (6) and equation (9), we have

$$\dot{\mathbf{x}}_1 = \Lambda \mathbf{x}_2, \quad (16)$$

where $\Lambda = \text{diag}(\mathbf{G}(\tilde{\sigma}), \mathbf{I})$. In terms of equation (8), equation (10), and equation (14), the integrated 6DOF error dynamics is derived as follows:

$$\mathbf{M} \dot{\mathbf{x}}_2 = \varsigma + \mathbf{B}(\xi + \Delta \xi) + \mathbf{d}, \quad (17)$$

where

$$\varsigma = \begin{bmatrix} -\omega^\times \mathbf{J} \omega + \mathbf{J}(\tilde{\omega}^\times \tilde{\mathbf{R}} \omega_d - \tilde{\mathbf{R}} \dot{\omega}_d) \\ -m \mathbf{C}_t \mathbf{v} - m \mathbf{n}_t - m \ddot{\mathbf{d}} \end{bmatrix}, \quad (18)$$

$$\mathbf{M} = \text{diag}(\mathbf{J}, m \mathbf{I}),$$

$$\mathbf{B} = \mathbf{D} \mathbf{A},$$

$$\mathbf{d} = [\tau_d^T, \mathbf{f}_d^T]^T. \quad (19)$$

3.3. Control Objective. Consider the 6DOF tracking error dynamics consisting of equation (16) and equation (17). Suppose that the full motion information of the desired

and the spacecraft is available to the spacecraft. The control objective is to design controller ξ for each thruster assembled in the spacecraft such that \mathbf{x}_1 and \mathbf{x}_2 converge to small sets around zero.

Assumption 1. The desired angular velocity ω_d and its derivative $\dot{\omega}_d$ are bounded. The desired position δ and its derivatives $\dot{\delta}$ and $\ddot{\delta}$ are bounded, respectively.

Assumption 2. \mathbf{J} and m are unknown constant parameters with known nominal values J_0 and m_0 , respectively.

4. Main Results

In this section, the main results are presented. An adaptive controller is first proposed such that the 6DOF tracking objective is realized. Then, the closed-loop stability analysis is undertaken.

4.1. Controller Development. In the following, an adaptive controller is synthesized by introducing a saturated RBFNN and a feasible auxiliary dynamical system, which results in the high accuracy tracking.

Define a variable

$$\mathbf{s} = \mathbf{x}_2 + \mathbf{K}_1 \mathbf{x}_1, \quad (20)$$

where $\mathbf{K}_1 = \text{diag}(\alpha_1 \mathbf{I}_3, \alpha_2 \mathbf{I}_3)$ with $\alpha_1 > 0$ and $\alpha_2 > 0$. In terms of equation (16) and equation (17), the derivative of equation (20) satisfies

$$\mathbf{M} \dot{\mathbf{s}} = \varsigma + \mathbf{B}(\xi + \Delta \xi) + \mathbf{d} + \mathbf{M} \mathbf{K}_1 \Lambda \mathbf{x}_2 = \rho + \mathbf{B} \xi + \mathbf{B} \Delta \xi + \mathbf{d}, \quad (21)$$

where $\rho = \varsigma + \mathbf{M} \mathbf{K}_1 \Lambda \mathbf{x}_2$.

Since the exact knowledge of inertial parameters cannot be obtained easily, we use their nominal values J_0 and m_0 to calculate the value of ρ . Define ρ_0 as the value of ρ when $\mathbf{J} = J_0$ and $m = m_0$. Let $\Delta \rho = \rho_0 - \rho$. It follows that

$$\mathbf{M} \dot{\mathbf{s}} = \rho_0 + \mathbf{B} \xi + \mathbf{B} \Delta \xi + \mathbf{d}^*, \quad (22)$$

where $\mathbf{d}^* = \mathbf{d} - \Delta \rho$. It can be easily known that \mathbf{d}^* consists of the variables $\mathbf{x}_1, \mathbf{x}_2, \dot{\omega}_d, \ddot{\delta}, \dot{\mathbf{v}}$, and $\ddot{\mathbf{v}}$. To approximate \mathbf{d}^* , we introduce the following RBFNN

$$\mathbf{d}^* = \mathbf{W}^T \Phi(\mathbf{y}) + \epsilon, \quad (23)$$

where $\mathbf{W} \in \mathbb{R}^{l \times 6}$ is the constant weight matrix, l is the number of nodes, $\Phi(\mathbf{y}) \in \mathbb{R}^l$ is the RBF vector, $\mathbf{y} = [\mathbf{x}_1^T, \mathbf{x}_2^T, \dot{\omega}_d^T, \ddot{\delta}^T, \dot{\mathbf{v}}^T, \ddot{\mathbf{v}}^T]^T$ is the input of the RBFNN, and $\epsilon \in \mathbb{R}^6$ is the approximation error. During the overshoot and transient at the beginning of the control process, large tracking errors may lead to large output of the RBFNN, which would increase the burden of the actuators. To overcome this disadvantage, we use a saturated RBFNN instead of the direct output from RBFNN. Let $\hat{\mathbf{W}}$ be the estimate of \mathbf{W} . Define $\Delta \epsilon = \text{sat}(\hat{\mathbf{W}}^T \Phi(\mathbf{y})) -$

$\hat{\mathbf{W}}^T \Phi(\mathbf{y})$ and the estimate error $\tilde{\mathbf{W}} = \hat{\mathbf{W}} - \mathbf{W}$, respectively. Then, we rewrite equation (23) as

$$\mathbf{d}^* = \text{sat}\left(\hat{\mathbf{W}}^T \Phi(\mathbf{y})\right) - \tilde{\mathbf{W}}^T \Phi(\mathbf{y}) + \epsilon^*, \quad (24)$$

where $\epsilon^* = \epsilon - \Delta\epsilon$.

Assumption 3. ϵ^* is bounded by an unknown constant $\bar{\epsilon}$, i.e., $|\epsilon^*| \leq \bar{\epsilon}$.

Let $\hat{\mathbf{W}}$ and $\hat{\epsilon}$ be the estimates of \mathbf{W} and $\bar{\epsilon}$, respectively. Design the following controller

$$\begin{aligned} \xi = \mathbf{B}^T (\mathbf{B}\mathbf{B}^T)^{-1} & \left(-\Lambda^T \mathbf{x}_1 - \mathbf{K}_2 \mathbf{s} - \rho_0 \right. \\ & \left. - \text{sat}\left(\hat{\mathbf{W}}^T \Phi(\mathbf{y})\right) - \frac{\hat{\epsilon} \mathbf{s}}{\|\mathbf{s}\| + \bar{\omega}} + \kappa_1 \mathbf{B} \chi \right), \end{aligned} \quad (25)$$

and the adaptation laws

$$\begin{aligned} \dot{\hat{\mathbf{W}}} &= \vartheta_1 (\Phi(\mathbf{y}) \mathbf{s}^T - \vartheta_2 \hat{\mathbf{W}}), \\ \dot{\hat{\epsilon}} &= \vartheta_3 \left(\frac{\|\mathbf{s}\|^2}{\|\mathbf{s}\| + \bar{\omega}} - \vartheta_4 (\hat{\epsilon} - \epsilon_0) \right), \end{aligned} \quad (26)$$

where $\mathbf{K}_2 = \text{diag}(\alpha_3 \mathbf{I}_3, \alpha_4 \mathbf{I}_3)$ with $\alpha_3 > 0$ and $\alpha_4 > 0$, $\kappa_1 > 0$, $\bar{\omega}$ is a small positive constant, ϑ_i , $i = 1, 2, 3, 4$, is a positive constant, ϵ_0 is the initial value of $\hat{\epsilon}$, and $\chi \in \mathbb{R}^N$ is an auxiliary signal generated from the following dynamical system

$$\dot{\chi} = -\kappa_2 \chi + \Delta \xi, \quad (27)$$

where $\kappa_2 > 0$.

By substituting equation (20) into equation (16), and equation (24) and (25) into equation (22), a 6DOF closed-loop system is derived as follows

$$\dot{\mathbf{x}}_1 = \Lambda(\mathbf{s} - \mathbf{K}_1 \mathbf{x}_1), \quad (28)$$

$$\begin{aligned} \mathbf{M} \dot{\mathbf{s}} &= -\Lambda^T \mathbf{x}_1 - \mathbf{K}_2 \mathbf{s} + \mathbf{B} \Delta \xi + \kappa_1 \mathbf{B} \chi \\ & - \tilde{\mathbf{W}}^T \Phi(\mathbf{y}) - \frac{\hat{\epsilon} \mathbf{s}}{\|\mathbf{s}\| + \bar{\omega}} + \epsilon^*. \end{aligned} \quad (29)$$

4.2. Stability Analysis. Since the controller for the 6DOF tracking error dynamics has been developed, we next focus on the closed-loop stability analysis. In particular, the following theorem summarizes the accomplishment of the 6DOF tracking objective.

Theorem 1. Consider the 6DOF closed-loop dynamics (28) and (29). Suppose that Assumptions 1–3 hold. If the control parameters are selected as

$$\begin{aligned} \min(\alpha_3, \alpha_4) &\geq \frac{\kappa_1}{4\theta_1} + \theta_2, \\ \kappa_2 &\geq \bar{\beta}\theta_1\kappa_1 + \theta_3, \end{aligned} \quad (30)$$

where θ_i , $i = 1, 2, 3$, is an arbitrary positive constant, and $\bar{\beta} = \sup(\|\mathbf{B}\|^2)$, the proposed controller (25) and adaptation laws (26) ensure that the 6DOF tracking objective is achieved, i.e., \mathbf{x}_1 and \mathbf{x}_2 converge to small sets around zero, respectively.

Proof. Define the estimate error $\tilde{\epsilon} = \hat{\epsilon} - \bar{\epsilon}$. Choose the following Lyapunov function candidate

$$V = \frac{1}{2} \mathbf{x}_1^T \mathbf{x}_1 + \frac{1}{2} \mathbf{s}^T \mathbf{M} \mathbf{s} + \frac{1}{2} \chi^T \chi + \frac{1}{2\vartheta_1} \text{tr}(\tilde{\mathbf{W}}^T \tilde{\mathbf{W}}) + \frac{1}{2\vartheta_3} \tilde{\epsilon}^2. \quad (31)$$

Its time derivative along equation (27), (28), and (29) satisfies

$$\begin{aligned} \dot{V} &= \mathbf{x}_1^T \dot{\mathbf{x}}_1 + \mathbf{s}^T \mathbf{M} \dot{\mathbf{s}} + \chi^T \dot{\chi} + \frac{1}{\vartheta_1} \text{tr}(\tilde{\mathbf{W}}^T \dot{\tilde{\mathbf{W}}}) + \frac{1}{\vartheta_3} \tilde{\epsilon} \dot{\tilde{\epsilon}} \\ &= -\mathbf{x}_1^T \Lambda \mathbf{K}_1 \mathbf{x}_1 - \mathbf{s}^T \mathbf{K}_2 \mathbf{s} - \kappa_2 \chi^T \chi + \kappa_1 \mathbf{s}^T \mathbf{B} \chi \\ & \quad + \mathbf{s}^T \mathbf{B} \Delta \xi + \chi^T \Delta \xi - \mathbf{s}^T \tilde{\mathbf{W}}^T \Phi(\mathbf{y}) - \frac{\hat{\epsilon} \mathbf{s}^T \mathbf{s}}{\|\mathbf{s}\| + \bar{\omega}} \\ & \quad + \mathbf{s}^T \epsilon^* + \frac{1}{\vartheta_1} \text{tr}(\tilde{\mathbf{W}}^T \dot{\tilde{\mathbf{W}}}) + \frac{1}{\vartheta_3} \tilde{\epsilon} \dot{\tilde{\epsilon}}. \end{aligned} \quad (32)$$

In view of $0 \leq \tilde{\sigma}^T \tilde{\sigma} \leq 1$ and $\tilde{\sigma}^T \mathbf{G}(\tilde{\sigma}) = (1 + \tilde{\sigma}^T \tilde{\sigma}) \tilde{\sigma}^T / 4$, we have

$$\mathbf{x}_1^T \Lambda \mathbf{K}_1 \mathbf{x}_1 = \mathbf{x}_1^T \begin{bmatrix} \frac{1 + \tilde{\sigma}^T \tilde{\sigma}}{4} \alpha_1 \mathbf{I}_3 & 0 \\ 0 & \alpha_2 \mathbf{I}_3 \end{bmatrix} \mathbf{x}_1 \geq c_1 \mathbf{x}_1^T \mathbf{x}_1, \quad (33)$$

where $c_1 = \min(\alpha_1/4, \alpha_2)$. Note that $\kappa_1 \mathbf{s}^T \mathbf{B} \chi \leq (\kappa_1/4\theta_1) \mathbf{s}^T \mathbf{s} + \bar{\beta}\theta_1 \kappa_1 \chi^T \chi$, $\mathbf{s}^T \mathbf{B} \Delta \xi \leq \theta_2 \mathbf{s}^T \mathbf{s} + \bar{\beta}/4\theta_2 \Delta \xi^T \Delta \xi$, $\chi^T \Delta \xi \leq \theta_3 \chi^T \chi + 1/4\theta_3 \Delta \xi^T \Delta \xi$. It follows that

$$\begin{aligned} \dot{V} &\leq -c_1 \mathbf{x}_1^T \mathbf{x}_1 - \left(\lambda_2 - \frac{\kappa_1}{4\theta_1} - \theta_2 \right) \mathbf{s}^T \mathbf{s} - (\kappa_2 - \bar{\beta}\theta_1 \kappa_1 \theta_3) \chi^T \chi \\ & \quad + \left(\frac{\bar{\beta}}{4\theta_2} + \frac{1}{4\theta_3} \right) \|\Delta \xi\|^2 - \mathbf{s}^T \tilde{\mathbf{W}}^T \Phi(\mathbf{y}) \\ & \quad + \frac{1}{\vartheta_1} \text{tr}(\tilde{\mathbf{W}}^T \dot{\tilde{\mathbf{W}}}) + \bar{\epsilon} \|\mathbf{s}\| - \frac{\hat{\epsilon} \mathbf{s}^T \mathbf{s}}{\|\mathbf{s}\| + \bar{\omega}} + \frac{1}{\vartheta_3} \tilde{\epsilon} \dot{\tilde{\epsilon}} \\ &\leq -c_1 \mathbf{x}_1^T \mathbf{x}_1 - c_2 \mathbf{s}^T \mathbf{s} - c_3 \chi^T \chi + \left(\frac{\bar{\beta}}{4\theta_2} + \frac{1}{4\theta_3} \right) \|\Delta \xi\|^2 \\ & \quad + \text{tr}\left(\tilde{\mathbf{W}}^T \left(\frac{1}{\vartheta_1} \dot{\tilde{\mathbf{W}}} - \Phi(\mathbf{y}) \mathbf{s}^T \right)\right) + \tilde{\epsilon} \left(\frac{1}{\vartheta_3} \dot{\tilde{\epsilon}} - \frac{\|\mathbf{s}\|^2}{\|\mathbf{s}\| + \bar{\omega}} \right), \end{aligned} \quad (34)$$

where $\lambda_2 = \min(\alpha_3, \alpha_4)$, $c_2 = \lambda_2 - \kappa_1/4\theta_1 - \theta_2$, $c_3 = \kappa_2 - \bar{\beta}\theta_1 \kappa_1 - \theta_3$. Substituting adaptation laws equation (26) gives

$$\begin{aligned} \dot{V} &\leq -c_1 \mathbf{x}_1^T \mathbf{x}_1 - c_2 \mathbf{s}^T \mathbf{s} - c_3 \chi^T \chi + \left(\frac{\bar{\beta}}{4\theta_2} + \frac{1}{4\theta_3} \right) \|\Delta \xi\|^2 \\ & \quad - \vartheta_2 \text{tr}(\tilde{\mathbf{W}}^T \hat{\mathbf{W}}) - \vartheta_4 \tilde{\epsilon} (\hat{\epsilon} - \epsilon_0). \end{aligned} \quad (35)$$

Note that $-\partial_2 \text{tr}(\tilde{\mathbf{W}}^T \tilde{\mathbf{W}}) \leq -\partial_2/2 \text{tr}(\tilde{\mathbf{W}}^T \tilde{\mathbf{W}}) + \partial_2/2 \text{tr}(\mathbf{W}^T \mathbf{W})$ and $-\partial_4 \tilde{\epsilon}(\tilde{\epsilon} - \epsilon_0) \leq -\partial_4/2 \tilde{\epsilon}^2 + \partial_4/2(\tilde{\epsilon} - \epsilon_0)^2$. Let $\bar{\Delta} = \sup \|\Delta \xi\|^2$. Then, we have

$$\dot{V} \leq -c_1 \mathbf{x}_1^T \mathbf{x}_1 - c_2 \mathbf{s}^T \mathbf{s} - c_3 \chi^T \chi - \frac{\partial_2}{2} \text{tr}(\tilde{\mathbf{W}}^T \tilde{\mathbf{W}}) - \frac{\partial_4}{2} \tilde{\epsilon}^2 + k^*, \quad (36)$$

where $k^* = (\bar{\beta}/4\theta_2 + 1/4\theta_3)\bar{\Delta} + \partial_2/2 \text{tr}(\mathbf{W}^T \mathbf{W}) + \partial_4/2(\bar{\epsilon} - \epsilon_0)^2 > 0$. In view of equation (31) and equation (36), then

$$\dot{V} \leq -c^* V + k^*, \quad (37)$$

where $c^* = \eta/\varphi > 0$, $\eta = \min\{c_1, c_2, c_3, \partial_2/2, \partial_4/2\}$, and $\varphi = 1/2 \max\{1, \lambda_{\max}(\mathbf{M}), 1/\partial_1, 1/\partial_3\}$. It follows that

$$V(t) \leq \left(V(0) - \frac{k^*}{c^*}\right) e^{-c^* t} + \frac{k^*}{c^*}. \quad (38)$$

So V eventually converges to $\Omega_V = \{V \mid V \leq \sqrt{k^*/c^*}\}$. It follows that $\mathbf{x}_1, \mathbf{x}_2, \chi, \tilde{\mathbf{W}}, \tilde{\epsilon}$ are bounded. In particular, let $\lambda_m = \lambda_{\min}(\mathbf{M})$ and $k_m = \max(\alpha_1, \alpha_2)$. With equation (20) and Ω_V , we can obtain that \mathbf{x}_1 and \mathbf{x}_2 eventually converge to $\Omega_1 = \{\mathbf{x}_1 \mid \|\mathbf{x}_1\| \leq \sqrt{2k^*/c^*}\}$ and $\Omega_2 = \{\mathbf{x}_2 \mid \|\mathbf{x}_2\| \leq (\sqrt{1/\lambda_m} + k_m)\sqrt{2k^*/c^*}\}$, respectively. This completes the proof.

Remark 1. Different from the conventional NN used in [12, 13, 16, 17], a saturated NN output is designed to reduce the large values caused by the large tracking errors during the overshoot and transient at the beginning of the control operation. An adaptive robust term is employed in the controller to compensate for the nonlinear term arising from the NN approximation error. The saturated NN and robust compensating term work together not only to counteract the dynamics uncertainties efficiently but also to improve the control accuracy.

Remark 2. In this paper, we can easily determine the controller parameters according to equation (30). Careful analysis implies that increasing $\alpha_j (j=1, 2, 3, 4)$ would result in a smaller set Ω_1 which illustrates that the ultimate convergent sets of $\tilde{\sigma}$ and $\tilde{\mathbf{r}}$ can be tuned by choosing appropriate control parameters. Moreover, larger control parameters could contribute to faster convergence rate but longer control saturation times which would bring the burden of thrusters. To this end, a reasonable compromise among practical control objectives is necessary.

5. Experimental Results

In this section, the hardware-in-the-loop experiments are tested to evaluate the proposed controller. The experiment scenario shows that a 3DOF simulator tracks a desired trajectory on the testbed surface while synchronizing its rotation angle with the desired attitude. First, basic hardware characteristics of the test facility are presented. Then, experimental results are illustrated by using the proposed controller.



FIGURE 1: The testbed facility: ASTERIX.

5.1. ASTERIX Facility Description. The hardware experimental validation of the proposed control strategy is conducted in the ASTERIX facility [19]. The test facility has three main elements including an operational arena, two 5DOF spaceflight simulators, and tracking (measurement) systems. An overview of this test facility is presented in Figure 1.

Some basic and important characteristics of the facility are listed as follows. A 6320 mm \times 3060 mm operational arena consists of four 3060 mm \times 1580 mm aluminum plates organized side by side. Due to the limitation of the manufacturing process, the inclination is inevitable. From the measurement by an SPI TRONIC PRO 3600, the maximum local inclination turned out to be -0.07° and the maximum local displacement with respect to the lowest point of the arena is 0.863 mm. The 5DOF spaceflight simulator consists of a 2DOF translation stage and a 3DOF attitude stage. The mass of each simulator is 147.22 kg, and the moment of inertia of the attitude stage presented in frame \mathcal{F}_{Bi} is

$$\mathbf{J} = \begin{bmatrix} 7.2002 & -0.0882 & -0.1230 \\ -0.0882 & 7.0141 & 0.0493 \\ -0.1230 & 0.0493 & 11.8319 \end{bmatrix} \text{ kg} \cdot \text{m}^2. \quad (39)$$

In addition, the spaceflight simulator is equipped with 3 reaction wheels and 16 thrusters. Each reaction wheel is set to provide torque around each axis of frame \mathcal{F}_{Bi} . The 16 thruster assemblies are symmetrically arranged with respect to the CR. Each set of four thrusters is set to expel exhaust gas in a fixed direction of the body frame, $\pm \mathbf{x}_{Bi}$ and $\pm \mathbf{y}_{Bi}$. The attitude of the simulator is obtained by an attitude and heading reference system (AHRS). The attitude measurement noise satisfies a random normal distribution

$$e_a^j = f(v_a^j) = \frac{1}{\sqrt{2\pi}\sigma_a^j} \exp\left(-\frac{(v_a^j - \mu_a^j)^2}{2(\sigma_a^j)^2}\right), \quad j = x, y, z, \quad (40)$$

TABLE 1: Desired trajectory.

Phase	Time (s)	x -axis r_{xd} (m)	y -axis r_{yd} (m)
1 st	$t \in \left[0, \frac{T}{2}\right]$	$0.6 \cos\left(\frac{4\pi}{T}t\right)$	$0.4 \sin\left(\frac{4\pi}{T}t\right)$
2 nd	$t \in \left[\frac{T}{2}, T\right]$	$0.45 \cos\left(\frac{4\pi}{T}t\right) + 0.15$	$0.3 \sin\left(\frac{4\pi}{T}t\right)$

TABLE 2: Thruster distribution.

Control direction	Number of each pair			
	1	2	3	4
$+\mathbf{x}_B$	F_1			F_{16}
$-\mathbf{x}_B$	F_4			F_{13}
$+\mathbf{y}_B$		F_5	F_{12}	
$-\mathbf{y}_B$		F_8	F_9	

where v_p^j is a random scalar, $\sigma_a = [\sigma_a^x, \sigma_a^y, \sigma_a^z]^T = [0.0175, 0.0170, 0.0347]^T$ deg, $\mu_a = [\mu_a^x, \mu_a^y, \mu_a^z]^T = [0.3, 0.3, 0.7]^T$ deg. The position of the simulator is measured by the tracking system. Similarly, the measurement error also satisfies the following random normal distribution

$$e_p = f(v_p) = \frac{1}{\sqrt{2\pi}\sigma_p} \exp\left(-\frac{(v_p - \mu_p)^2}{2\sigma_p^2}\right), \quad (41)$$

where v_p is a random scalar, $\sigma_p = 0.2950 \times 10^{-3}$ m, and $\mu_p = -19.7499 \times 10^{-6}$ m.

5.2. Experimental Results. In this subsection, we show the experimental results.

The desired rotation angle is governed as

$$\psi_d = \psi(0) - \frac{\psi(0)}{T}t(\text{deg}), \quad (42)$$

where $\psi(0)$ is the initial angle of the simulator and T is the time of the experiment. The desired trajectory in each phase is given in Table 1.

In this experiment, we use 4 pairs of thrusters generating the control efforts. The distribution of thrusters are shown in Table 2 and Figure 2. The distribution matrix is given by $\mathbf{A} = [l, l, -l, -l; 1, 0, 0, 1; 0, 1, 1, 0]$, where l is the arm of force of each pair of thrusters. The model parameters of the simulator are listed in Table 3, respectively.

The saturation constraints of the NN with $l = 80$ nodes are chosen as $\mathbf{a} = \mathbf{b} = [0.2, 0.8, 0.8]^T$. The parameter estimates are initialized as $\hat{\mathbf{W}}(0) = 0$ and $\hat{e}(0) = 1$. The parameters of the controller and adaptation laws are chosen as $\kappa_1 = \kappa_2 = 0.1$, $\vartheta_1 = 0.025$, $\vartheta_2 = 0.01$, $\vartheta_3 = 0.03$, $\vartheta_4 = 0.01$, and $\hat{\omega} = 0.01$. The experiment time is $T = 270$ (s). Four groups of experiments are performed by using different control parameters and nominal values of inertial parameters which are summa-

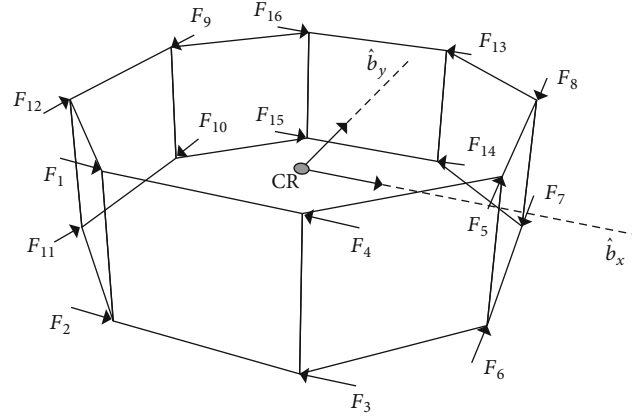


FIGURE 2: Distribution of the thrusters.

TABLE 3: Model parameters.

Parameter	Value	Unit
Mass m	147.22	kg
Moment of inertia j_z	11.8319	kg · m ²
Gravitational acceleration g	9.8	m/s ²
Arm of force l	0.4875	M
Magnitude constraint $\bar{\xi}_i^+$ ($i = 1, 5, 12, 16$)	1, 1, 1, 1	N
Magnitude constraint $\bar{\xi}_j^-$ ($j = 4, 8, 9, 13$)	1, 1, 1, 1	N

TABLE 4: Control parameters and nominal values.

Case	Control parameter	Nominal value
1	$\alpha_1 = 4, \alpha_2 = 11, \alpha_3 = 4, \alpha_4 = 6$	$0.65M$
2	$\alpha_1 = 4, \alpha_2 = 10, \alpha_3 = 4, \alpha_4 = 6$	$0.9M$
3	$\alpha_1 = 4, \alpha_2 = 2, \alpha_3 = 4, \alpha_4 = 4$	$1.3M$
4	$\alpha_1 = 4, \alpha_2 = 2, \alpha_3 = 4, \alpha_4 = 4$	$1.75M$

rized in Table 4, where $M = \text{diag}(j_z, m, m)$. Experimental results are presented in Figures 3–10.

Figure 3 collects the rotation angle error of each case. Figure 4 presents the trajectory of each case versus the desired. Figures 5 and 6 show the position tracking errors in x -axis and y -axis of each case, respectively. Table 5 summarizes all the standard derivations of tracking errors in different cases. From the experimental results, it can be seen that the simulator tracks the desired trajectory while synchronizing its rotation angle with a good performance in spite of measurement errors and a large range of parameter uncertainty. During the first phase of the experiment, the transient behavior arises because the initial position of the simulator does not coincide with the initial value of the desired trajectory. After that, the simulator tracks the desired trajectory fairly well. Apart from the slight discrepancy of the tracking errors, the high control accuracy is confirmed by the experimental results in spite of the parameter uncertainty from -35% and $+75\%$.

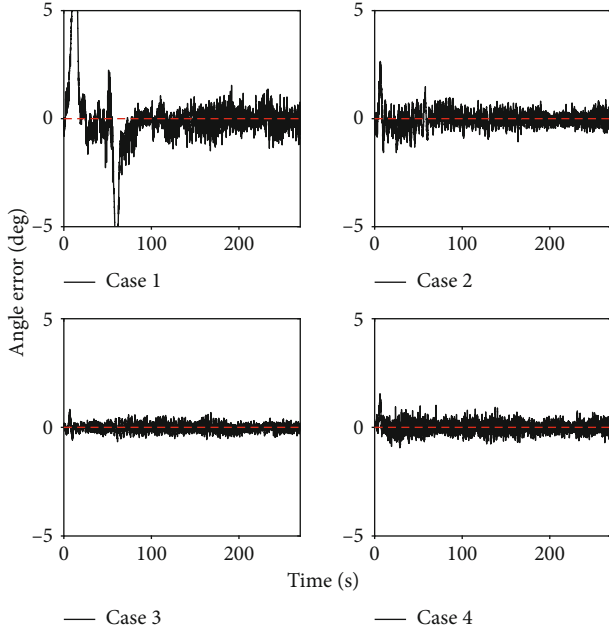


FIGURE 3: Experimental result: angle errors.

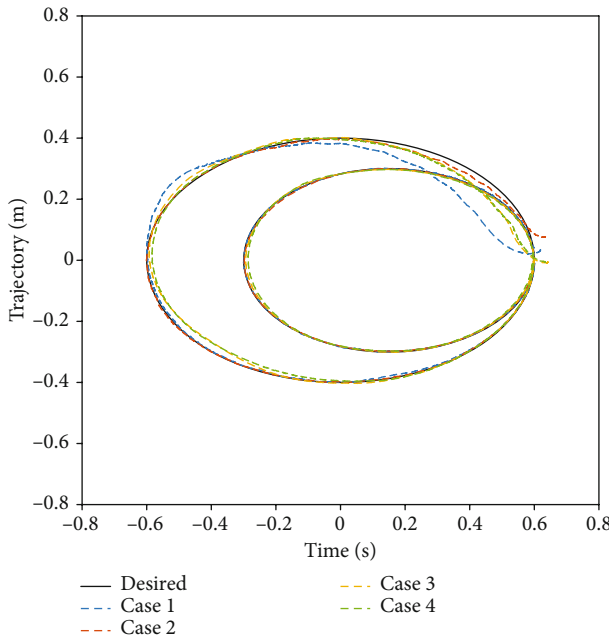
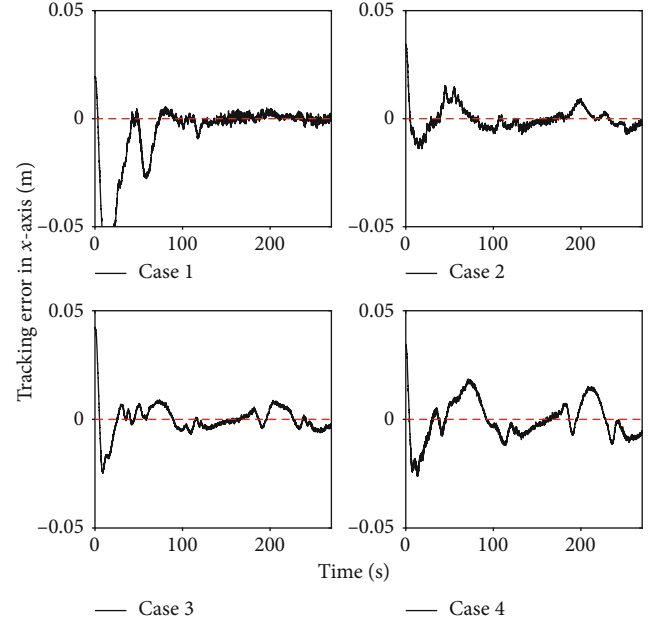
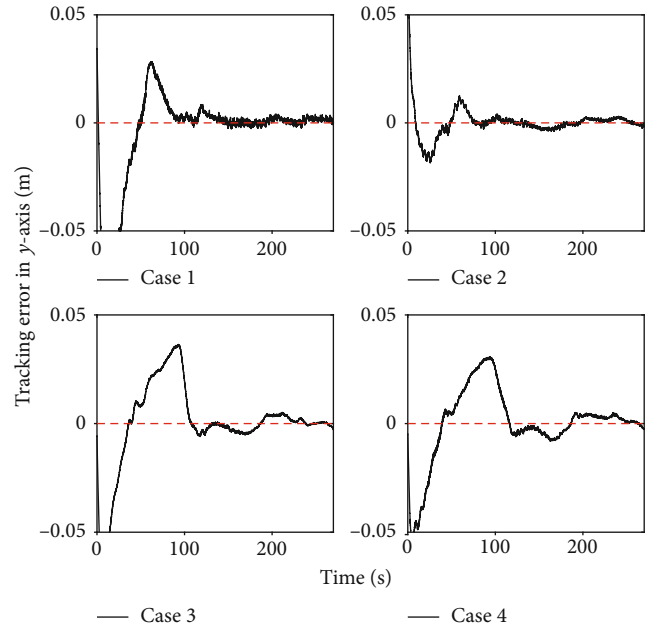


FIGURE 4: Experimental result: trajectory of simulator.

We next show the detailed experimental result of Case 2 to evaluate the proposed controller. Figure 7 illustrates the top view of the experiment result, where the orange line is the initial position with an x -axis in frame \mathcal{F}_B representing initial angle of the simulator and the blue line is the final position of the simulator. From this result, we can see that the simulator tracks the desired trajectory with a good performance. In particular, there is no obvious tracking error after the simulator enters the second phase. In addition, the command control of each thruster is collected in Figure 8. It can

FIGURE 5: Experimental result: tracking error of simulator in x -axis.FIGURE 6: Experimental result: tracking error of simulator in y -axis.

be seen that all the control signals are within their magnitude constraints, respectively. Besides, Figure 9 describes the output of the NN versus time, and Figure 10 presents the estimate \hat{e} and norm of the auxiliary signal χ versus time, respectively. At the beginning of the experiment, it can be seen that the output of the NN is much larger than the magnitude constraint of the thruster. Instead, the saturated value is applied in the controller which contributes to reduce the burden of the thrusters. It is also evidenced that the estimate \hat{e} and auxiliary signal χ remain bounded during the experiment.

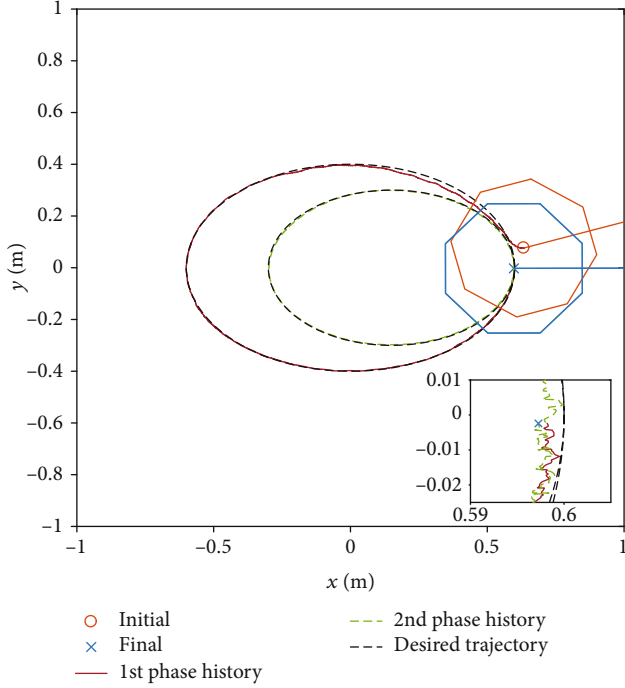


FIGURE 7: Experimental result: attitude and position of simulator in Case 2.

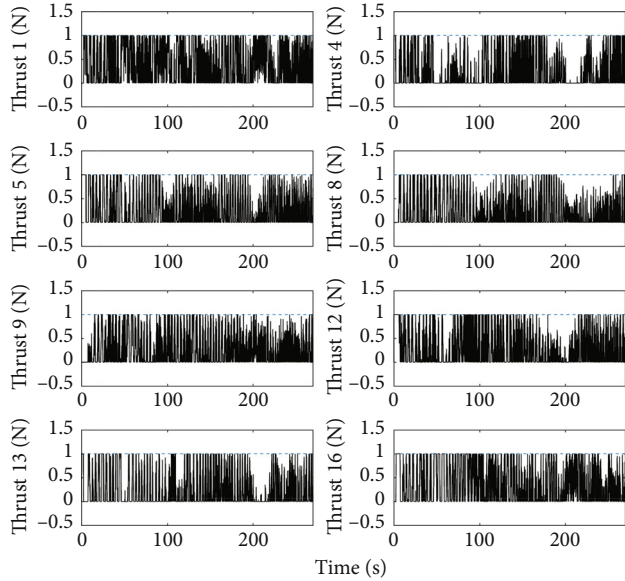


FIGURE 8: Experimental result: command control force of each thruster in Case 2.

6. Conclusions

We develop an NN-based saturated adaptive controller for 6DOF spacecraft tracking operations in this paper. To estimate the dynamics uncertainties with high accuracy while avoiding the long time control saturation during the initial operation, an adaptive saturated NN is designed with its approximate error being compensated by a continuous robust term. An auxiliary dynamical system is introduced

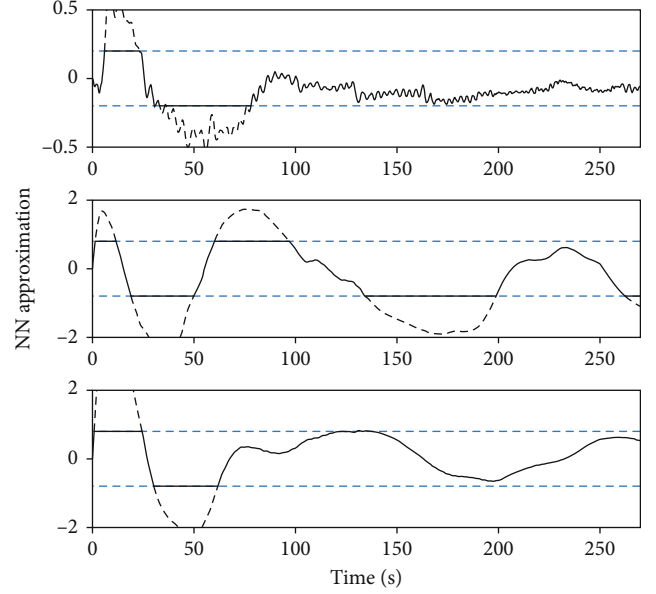


FIGURE 9: Experimental result: output of NN in Case 2.

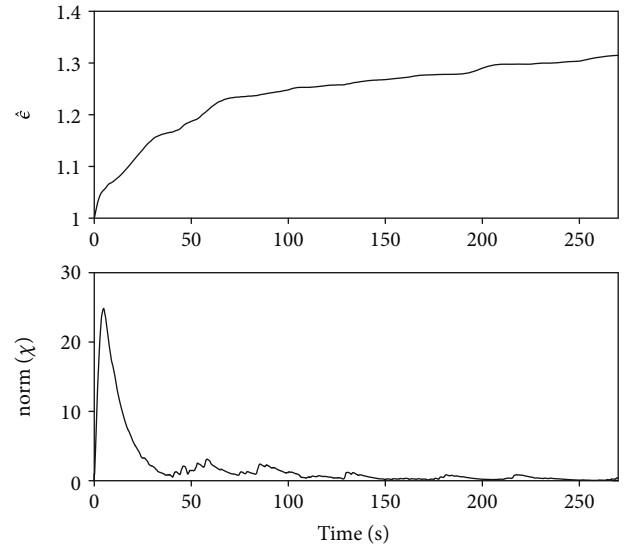


FIGURE 10: Experimental result: estimate value and auxiliary signal in Case 2.

TABLE 5: Standard derivations of tracking errors.

Case	1-2 phases			2 nd phase		
	ψ (deg)	\tilde{r}_x (mm)	\tilde{r}_y (mm)	ψ (deg)	\tilde{r}_x (mm)	\tilde{r}_y (mm)
1	1.7275	16.8991	23.5340	0.4100	1.5233	1.2869
2	0.3983	5.7777	7.6600	0.2551	3.4071	1.7211
3	0.1810	7.1407	19.7165	0.1657	3.8055	2.7741
4	0.2636	9.3525	17.0123	0.2183	7.2070	3.7914

to overcome the effects caused by control saturation. The ultimate boundedness of the closed-loop dynamics has been proved. Hardware-in-the-loop experimental validation is conducted on the test facility ASTERIX, where a 3DOF

tracking scenario of the planar and rotational maneuver is performed in the presence of unknown inertial parameters, disturbances, and measurement errors. Experimental results demonstrate that the proposed controller ensures the simulator tracking a desired trajectory with a good performance and that the rotation angle and position tracking errors are within 0.5 degree and 8 millimeter during the final phase.

Data Availability

The simulation data used to support the findings of this study are available from the corresponding author upon request.

Conflicts of Interest

The authors declare that they have no conflicts of interest.

Acknowledgments

This work was supported by KASI (Korea Astronomy and Space Science Institute) and Yonsei research collaboration program for the frontiers of astronomy and space science. This work was also supported by the Space Basic Technology Development Program through the National Research Foundation of Korea funded by the Ministry of Science and ICT of Republic of Korea (2018MIA3A3A02065610).

References

- [1] M. Ciarcia, R. Cristi, and M. Romano, "Emulating scaled Clohessy-Wiltshire dynamics on an air-bearing spacecraft simulation testbed," *Journal of Guidance, Control, and Dynamics*, vol. 40, no. 10, pp. 2496–2510, 2017.
- [2] R. Kristiansen, P. J. Nicklasson, and J. T. Gravdahl, "Spacecraft coordination control in 6DOF: integrator backstepping vs passivity-based control," *Automatica*, vol. 44, no. 11, pp. 2896–2901, 2008.
- [3] R. Kristiansen and P. J. Nicklasson, "Spacecraft formation flying: a review and new results on state feedback control," *Acta Astronautica*, vol. 65, no. 11–12, pp. 1537–1552, 2009.
- [4] H. Sun, S. Li, and S. Fei, "A composite control scheme for 6DOF spacecraft formation control," *Acta Astronautica*, vol. 69, no. 7–8, pp. 595–611, 2011.
- [5] Q. Li, J. Yuan, B. Zhang, and H. Wang, "Disturbance observer based control for spacecraft proximity operations with path constraint," *Aerospace Science and Technology*, vol. 79, pp. 154–163, 2018.
- [6] N. Filipe and P. Tsiotras, "Adaptive position and attitude-tracking controller for satellite proximity operations using dual quaternions," *Journal of Guidance, Control, and Dynamics*, vol. 38, no. 4, pp. 566–577, 2015.
- [7] F. Zhang and G. Duan, "Robust adaptive integrated translation and rotation control of a rigid spacecraft with control saturation and actuator misalignment," *Acta Astronautica*, vol. 86, pp. 167–187, 2013.
- [8] K. Xia and W. Huo, "Adaptive control for spacecraft rendezvous subject to actuator faults and saturations," *ISA Transactions*, vol. 80, pp. 176–186, 2018.
- [9] K. Xia and W. Huo, "Disturbance observer based fault-tolerant control for cooperative spacecraft rendezvous and docking with input saturation," *Nonlinear Dynamics*, vol. 88, no. 4, pp. 2735–2745, 2017.
- [10] L. Sun and Z. Zheng, "Disturbance observer-based robust saturated control for spacecraft proximity maneuvers," *IEEE Transactions on Control Systems Technology*, vol. 26, no. 2, pp. 684–692, 2018.
- [11] S. S. Ge, C. C. Hang, T. H. Lee, and T. Zhang, *Stable Adaptive Neural Network Control*, Kluwer, Norwell, MA, 2001.
- [12] J. Bae and Y. Kim, "Adaptive controller design for spacecraft formation flying using sliding mode controller and neural networks," *Journal of the Franklin Institute*, vol. 349, no. 2, pp. 578–603, 2012.
- [13] K. Xia and W. Huo, "Robust adaptive backstepping neural networks control for spacecraft rendezvous and docking with input saturation," *ISA Transactions*, vol. 62, pp. 249–257, 2016.
- [14] K. Subbarao and S. Welsh, "Nonlinear control of motion synchronization for satellite proximity operations," *Journal of Guidance, Control, and Dynamics*, vol. 31, no. 5, pp. 1284–1294, 2008.
- [15] L. Sun and W. Huo, "6-DOF integrated adaptive backstepping control for spacecraft proximity operations," *IEEE Transactions on Aerospace and Electronic Systems*, vol. 51, no. 3, pp. 2433–2443, 2015.
- [16] Y. Zou and Z. Zheng, "A robust adaptive RBFNN augmenting backstepping control approach for a model-scaled helicopter," *IEEE Transactions on Control Systems Technology*, vol. 23, no. 6, pp. 2344–2352, 2015.
- [17] Z. Zheng and L. Sun, "Path following control for marine surface vessel with uncertainties and input saturation," *Neurocomputing*, vol. 177, pp. 158–167, 2016.
- [18] T. Rybus and K. Seweryn, "Planar air-bearing microgravity simulators: review of applications, existing solutions and design parameters," *Acta Astronautica*, vol. 210, pp. 239–259, 2016.
- [19] Y. Eun, S.-Y. Park, and G.-N. Kim, "Development of a hardware-in-the-loop testbed to demonstrate multiple spacecraft operations in proximity," *Acta Astronautica*, vol. 147, pp. 48–58, 2018.
- [20] P. Tsiotras, "ASTROS: a 5DOF experimental platform for research in spacecraft proximity operations," in *AAS Guidance and Control Conference*, Breckenridge, Colorado, USA, 2014.
- [21] S. Ulrich, A. Saenz-Otero, and I. Barkana, "Passivity-based adaptive control of robotic spacecraft for proximity operations under uncertainties," *Journal of Guidance, Control, and Dynamics*, vol. 39, no. 6, pp. 1441–1450, 2016.
- [22] G. Guglieri, F. Maroglio, P. Pellegrino, and L. Torre, "Design and development of guidance navigation and control algorithms for spacecraft rendezvous and docking experimentation," *Acta Astronautica*, vol. 94, no. 1, pp. 395–408, 2014.
- [23] L. Guarnaccia, R. Bevilacqua, and S. P. Pastorelli, "Suboptimal LQR-based spacecraft full motion control: theory and experimentation," *Acta Astronautica*, vol. 122, pp. 114–136, 2016.
- [24] M. Wilde, M. Ciarcià, A. Grompone, and M. Romano, "Experimental characterization of inverse dynamics guidance in docking with a rotating target," *Journal of Guidance, Control, and Dynamics*, vol. 39, no. 6, pp. 1173–1187, 2016.
- [25] J. Virgili-Llop, C. Zagaris, H. Park, R. Zappulla, and M. Romano, "Experimental evaluation of model predictive control and inverse dynamics control for spacecraft proximity and docking maneuvers," *CEAS Space Journal*, vol. 10, no. 1, pp. 37–49, 2018.

- [26] R. Zappulla II, J. Virgili-Llop, C. Zagaris, H. Park, and M. Romano, "Dynamic air-bearing hardware-in-the-loop testbed to experimentally evaluate autonomous spacecraft proximity maneuvers," *Journal of Spacecraft and Rockets*, vol. 54, no. 4, pp. 825–839, 2017.
- [27] H. Schaub and J. L. Junkins, *Analytical Mechanics of Space Systems*, AIAA Education Series, American Institute of Aeronautics and Astronautics, Inc., Reston, VA, USA, 2003.
- [28] R. Kristiansen, E. I. Grøtli, P. J. Nicklasson, P. J. Nicklasson, and J. T. Gravdahl, "A model of relative translation and rotation in leader-follower spacecraft formations," *Modeling, Identification and Control*, vol. 28, no. 1, pp. 3–14, 2007.

